The value of metal artifact reduction and iterative algorithms in dual energy CT angiography in patients after complex endovascular aortic aneurysm repair

Wojciech Kazimierczak [a,b,c,*], Ewa Nowak [b], Natalia Kazimierczak [c], Tomasz Jankowski [d], Agnieszka Jankowska [d], Zbigniew Serafin [a,b]

[a] *Collegium Medicum, Nicolaus Copernicus University in Torun, Jagiellońska 13-15, 85-067, Bydgoszcz, Poland*
[b] *University Hospital No 1 in Bydgoszcz, Marii Skłodowskiej – Curie 9, 85-094, Bydgoszcz, Poland*
[c] *Kazimierczak Private Medical Practice, Dworcowa 13/u6a, 85-009, Bydgoszcz, Poland*
[d] *Jankowsci Private Dental Practice, Czerwonego Krzyża 24, 68-200, Żary, Poland*

A B S T R A C T

Rationale and objectives: Evaluation of the diagnostic value of linearly blended (LB) and virtual monoenergetic images (VMI) reconstruction techniques with and without metal artifacts reduction (MAR) and of adaptive statistical iterative reconstructions (ASIR) in the assessment of target vessels after branched/fenestrated endovascular aortic repair (f/brEVAR) procedures.
Materials and methods: CT scans of 28 patients were used in this study. Arterial phase of examination was obtained using a dual-energy fast-kVp switching scanner. CT numbers in the aorta, celiac trunk, superior mesenteric artery, and renal arteries were measured in the following reconstructions: LB, VMI 60 keV, VMI MAR 60 keV, VMI ASIR 60 % 60 keV. Contrast-to-noise ratio (CNR) and signal-to-noise ratio (SNR) were calculated for each reconstruction. Luminal diameters (measurements at 2 levels of stent) and subjective image quality (5-point Likert scale) were assessed (2 readers, blinded to the type of reconstruction).
Results: The highest mean values of CNR and SNR in vascular structures were obtained in VMI MAR 60 keV (CNR 12.526 ± 2.46, SNR 17.398 ± 2.52), lower in VMI 60 keV (CNR 11.508 ± 2.01, SNR 16.524 ± 2.07) and VMI ASIR (CNR 11.086 ± 1.78, SNR 15.928 ± 1.82), and the lowest in LB (CNR 6.808 ± 0.79, SNR 11.492 ± 0.79) reconstructions. There were no statistically significant differences in the measurements of the stent width between reconstructions (p > 0.05). The highest subjective image quality was obtained in the ASIR VMI (4.25 ± 0.44) and the lowest in the MAR VMI (1.57 ± 0.5) reconstruction.
Conclusion: Despite obtaining the highest values of SNR and CNR in the MAR VMI reconstruction, the subjective diagnostic value was the lowest for this technique due to significant artifacts. The type of reconstruction did not significantly affect vessel diameter measurements (p > 0.05). Iterative reconstructions raised both objective and subjective image quality.

* Corresponding author. Dworcowa 13/u6a, 85-009, Bydgoszcz, Poland.
  E-mail address: wojtek.kazimierczak@gmail.com (W. Kazimierczak).

Abbreviations

LB	linearly blended
VMI	virtual monoenergetic images
MAR	metal artifact reduction
ASIR	Adaptive Statistical Iterative Reconstructions
f/brEVAR	fenestrated/branched Endovascular Aneurysm Repair
CNR	Contrast – to – Noise Ratio
SNR	Signal – to- Noise Ratio
AAA	Abdominal Aortic Aneurysm
SMA	Superior Mesenteric Artery
TC	Celiac Trunk
CTA	Compute Tomography Angiography
DECTA	Dual-Energy Computed Tomography Angiography
AI	Artifact Index
MPR	Multiplanar Reconstruction
RRA	Right Renal Artery
LRA	Left Renal Artery
SD	Standard Deviation
RCIA	Right Common Iliac Artery
ICC	Interclass Correlation Coefficient
CI	Confidence Interval

1. Introduction

Abdominal aortic aneurysms (AAAs) are a common medical condition [1] and one of the main causes of death in developed countries [2]. Endovascular aortic repair (EVAR) is currently the principal treatment method for AAAs [3]. Use of fenestrated and branched stent–grafts in EVAR (f/bEVAR) allows repair procedures of juxtarenal and thoracoabdominal aneurysms. However, due to the potential life-threating complications, EVAR patients need lifelong diagnostic surveillance [3,4].

A successful f/brEVAR procedure is defined as completed with exclusion of the aneurysm sac from circulation, preserved patency of the stent–graft and its branches, and no endoleaks (except type II endoleaks) [5]. Higher complexity of the procedure and device requires the use of additional stent–grafts supplying the celiac and mesenteric arteries, which results in a higher frequency of complications [6]. Target vessel stenosis and occlusion is a complication responsible for 23.5 % of repeated interventions following f/brEVAR procedures [7]. Stenosis of the superior mesenteric artery (SMA) or the celiac trunk (TC) can lead to potentially life-threating consequences [5]. In most cases, significant stenosis (blockage of >50 % of the vessel lumen [8]) and occlusion of the blood vessel occurs gradually through progressing occult stenosis. In some cases, stenosis is due to a kink in the target artery stent, unrecognized intraoperatively. The phenomenon emphasizes the need for a careful assessment of the target vessel stents using diagnostic imaging.

Computed tomography angiography (CTA) is the main diagnostic technique used in the follow-up of patients after EVAR [9]. Its modification, dual-energy CTA (DECTA), has demonstrated a high diagnostic value in patients after EVAR and those with various cardiovascular conditions [10,11]. Several papers have been published in which a high diagnostic value of DECTA is demonstrated, e. g. in the detection of pulmonary embolism [12,13], assessment of the coronary vasculature and functional evaluation of the myocardium [14,15], differentiation of venous thrombosis from iodine flux artifacts [16], active arterial bleeding [17], radiation decreasing the contrast volume [18], radiation dose reduction [19,20].

DECT allows reconstruction of Virtual Monoenergetic Images (VMIs) to enhance the contrast of intravascular iodine and surrounding tissues, improving the diagnostic value of the examination in terms of, e.g., assessment of vascular stenosis, detection of endoleaks, post-procedural assessment of thoracic aorta [9,21–28]. Use of monoenergetic reconstructions with low photon energies (40–60 keV) permits obtaining very high attenuation values associated with the properties of the K absorption curve characteristic of iodine [29]. However, such reconstructions contain a high level of image noise which decreases the contrast-to-noise ratio (CNR) and potentially reduces the diagnostic value of images. The use of high-keV VMI reconstructions (≥100 keV) allows reducing blooming artifacts caused by hyperdense structures (i.e. calcified plaques, metal stents), which is particularly useful in cardiac-CT [30]. Reconstructions in the range of 130–150 keV allow optimal imaging of the lumen of stents of <3 mm in diameter, with a potential concurrent reduction of ionizing radiation dose [31,32]. Moreover, these reconstructions improve the diagnostic value of examinations plagued with artifacts associated with calcified plaques and contrast material influx [33,34].

Adaptive statistical iterative reconstruction (ASIR, GE Healthcare, Milwaukee, WI, USA) is one of the methods aimed to decrease noise and improve image quality. Such reconstructions allow reducing image noise and artifacts, as well as improving diagnostic confidence and increasing the conspicuity of subtle abdominal lesions and cardiovascular conditions [35–38].

In addition to image noise, artifacts associated with stent–graft elements or past endovascular procedures (e.g. coils after endoleak treatment) also negatively affect the diagnostic value of CTA images. These artifacts hamper the visualization of endoleaks and stent

lumen, reducing diagnostic accuracy [39–42]. The basic methods of metal artifact reduction (MAR) include the MAR algorithms, iterative techniques and dual energy tomography [43]. Use of VMI with a high photon energy range alongside the MAR algorithms has shown a high diagnostic value in assessing orthopedic implants [43,44]. Only a few studies of the effect of MAR on the CTA diagnostic value in assessing endoleaks [42] and the patency of stents following f/brEVAR [41] have been conducted to date. To our knowledge, there have been no studies comparing various reconstruction techniques in the assessment of stents in target vessels after f/brEVAR.

The aim of the study was to evaluate several VMI reconstruction techniques with and without MAR and ASIR reconstructions in the assessment of target vessels after f/brEVAR procedures.

2. Materials and methods

2.1. Population

The study involved 28 patients (5 women, 23 men, mean age 72,1, range 62.9–86.9) after a f/brEVAR procedure, referred for 28 CTAs performed in the period from August 2019 to December 2020. The ethics committee of our University approved this prospective study, and all patients provided their written informed consent. A follow-up examination was conducted in every patient 1 month after stent–graft implantation. The exclusion criteria were: known adverse reactions to iodinated contrast media and impaired renal function (glomerular filtration rate <30 mL/min).

2.2. CT scanning protocol and image reconstruction

All CT scans were obtained using a dual-energy fast-kVp switching scanner (Discovery 750 HD, GE Healthcare, Wisconsin, USA). The standard examination protocol consisted of three phases: one non-enhanced and two post-contrast dual-energy acquisitions – arterial and delayed-phase. The arterial phase was acquired with the use of the GSI-40 preset, with the following scan parameters: helical, 0.8 s tube rotation time, 40 mm detector coverage, pitch factor: 0.985:1, 35 cm DFOV. An intravenous administration of 80 mL of Ominpaque 350 (GE Healthcare) non-ionic iodine contrast to the peripheral vein at a rate of 4 mL/min was performed. The contrast agent was followed by saline bolus chaser. A bolus tracking tool was used, triggering the start of arterial acquisition once 125 HU was exceeded in the region of interest (ROI) positioned in the proximal descending aorta. The delayed phase was performed automatically 60 s after the onset of the arterial phase.

All measurements and reconstructions were performed on a dedicated GE Healthcare console (GSI Viewer, Advantage Workstation Release 4.7, GE Healthcare). Images were reconstructed for further analysis using linear blending (70 % 140 kVp, 30 % 80 kVp), VMI, ASIR 60 % VMI, MAR VMI. All VMI image series were reconstructed at energy levels from 40 to 90 keV (with 10 keV increments).

2.3. Assessment of objective image quality

Circular regions of interest (ROIs) were placed in the aortic lumen at the level of the main stent–graft module, visceral adipose tissue, one of the psoas muscles, celiac trunk (TC), superior mesenteric artery (SMA), right renal artery (RRA), left renal artery (LRA). An automatic ROI propagation tool was used. The ROIs were placed in the aorta and in the lumen of the stents in target vessels in two areas – one with no artifacts and one containing the worst artifacts. An automatic ROI propagation tool was used, "cloning" ROIs in all of the investigated reconstructions. All measurements were performed by scaling an ROI as large as possible without including calcifications, plaques, vessel borders or stent material. The mean ROI sizes were 69 mm^2 in the aorta, 252 mm^2 in the adipose tissue, 151 mm^2 in the psoas muscle and 4 mm^2 in stents in target vessels.

Mean attenuation and image noise defined as standard deviation (SD) in the subcutaneous adipose tissue were registered. Contrast-to-noise ratio (CNR) was calculated using formula 1.

Formula 1. Contrast to noise ratio.

$$\mathbf{CNR} = \left(A_A - A_p \right) / N$$

Signal-to-noise ratio (SNR) was calculated using formula 2.

Formula 2. Signal to noise ratio.

$$\mathbf{SNR} = A_A / N$$

In both formulas 1 & 2: A_A is the mean attenuation of the artery lumen (aorta, common iliac artery), A_p is the mean attenuation of the psoas muscle, N is noise (SD in the visceral adipose tissue).

The differentiation between the mean attenuation at the worst artifacts and the standard CT numbers (part of vessel without artifacts) were calculated using formula 3.

Formula 3. ΔCT

$$\mathbf{\Delta CT} = CT_{maxartifact} - CT_{standard}$$

To quantify severity of artifacts, the Artifat Index (AI) was calculated using formula 4.

Formula 4. Artifact index

Table 1
Objective image quality in the aorta and stents – no-artifact and maximum-artifact areas.

Parameter		LB (A)		VMI 60 (B)		MAR VMI 60 (C)		ASIR 60 % VMI 60 (D)		P	
		No artifacts	Max. artifacts	No artifacts	Max. artifacts	No artifacts	Max. artifacts	No artifacts	Max. artifacts	No artifacts	Max. artifacts
CT attenuation, HU	Aorta	296.75 ± 56.74	296.65 ± 56.63	485.22 ± 93.52	480.13 ± 97.6	496.25 ± 94.51	499.56 ± 118.92	486.58 ± 93.52	480 ± 97.58	p < 0.001; C,B>A D > B,A	p < 0.001; C,B,D > A
	TC	313.47 ± 73.63	349.61 ± 171.47	490.77 ± 115.46	553.38 ± 233.44	565.36 ± 169.28	586.3 ± 239.36	494.6 ± 115.43	556.65 ± 229.47	p < 0.001; C,D,B > A	p = 0.001; C,D,B > A
	SMA	324.13 ± 63.81	397.4 ± 196.33	514.88 ± 101.47	615.28 ± 240.52	545.72 ± 115.96	654.8 ± 182.63	519.38 ± 101.27	624.07 ± 248.73	p < 0.001; C,D,B > A	p < 0.001; C,D,B > A
	RRA	353.96 ± 82.04	390.31 ± 117.35	581.32 ± 124.36	653.82 ± 214.08	598.79 ± 134.73	728.71 ± 211	585.27 ± 128.18	616 ± 163.17	p < 0.001; C,D,B > A	p < 0.001; C,B,D > A
	LRA	358.05 ± 93.16	373.94 ± 102.52	573.53 ± 134.01	593.34 ± 167.15	634.28 ± 205.84	643.32 ± 224.76	581.42 ± 138.92	588.99 ± 171.47	p < 0.001; C,D,B > A	p < 0.001; C,B,D > A
Noise		30.96 ± 10.57	29.5 ± 6.33	37.11 ± 10.45	37.23 ± 10.8	38.44 ± 11.08	37.93 ± 10.39	38.48 ± 11.05	38.53 ± 11.4	p < 0.001; B>A D,C > B,A	p < 0.001; C,B>A D > B,A
CNR	Aorta	5.81 ± 4.22	4.53 ± 4.26	10.52 ± 5.63	9.23 ± 5.61	10.53 ± 5.91	9.64 ± 6.05	10.24 ± 5.6	8.97 ± 5.45	p < 0.001; C,D>A B > D,A	p < 0.001; C,D>A B > D,A
	TC	6.34 ± 4.42	6.12 ± 6.77	10.71 ± 6.26	10.71 ± 7.5	12.21 ± 7.24	11.46 ± 8.25	10.46 ± 6.22	10.46 ± 7.12	p < 0.001; C,D>A B > D,A	p = 0.005; C,B,D > A
	SMA	6.78 ± 4.26	8.1 ± 7.96	11.39 ± 5.55	13.38 ± 9.58	11.71 ± 5.74	13.92 ± 7.78	11.11 ± 5.41	13.26 ± 9.61	p < 0.001; C,B,D > A	p = 0.001; C,B,D > A
	RRA	7.89 ± 5.05	7.64 ± 5.11	13.41 ± 6.54	13.86 ± 6.6	13.22 ± 6.75	15.98 ± 8.27	13.08 ± 6.63	12.59 ± 5.98	p < 0.001; B,C,D > A	p < 0.001; C,D>A B > D,A
	LRA	7.22 ± 4.3	5.94 ± 4.47	12.36 ± 5.54	10.36 ± 6.11	13.71 ± 8.44	11.63 ± 8.56	12.15 ± 5.58	10.15 ± 6.91	p < 0.001; C,B,D > A	p = 0.001; C,B,D > A
SNR	Aorta	10.49 ± 3.43	10.66 ± 3.73	14.37 ± 5.37	14.24 ± 5.97	14.26 ± 5.66	14.49 ± 6.26	13.97 ± 5.4	13.8 ± 5.8	p < 0.001; C,D>A B > D,A	p < 0.001; C,D>A B > D,A
	TC	11.03 ± 3.99	12.25 ± 6.19	14.56 ± 6.31	15.71 ± 7.46	15.94 ± 7.18	16.32 ± 8.38	14.18 ± 6.3	15.29 ± 7.03	p < 0.001; C,D>A B > D,A	p = 0.031; B,D > A
	SMA	11.46 ± 3.83	14.22 ± 7.75	15.23 ± 5.41	18.38 ± 10.1	15.44 ± 5.49	18.78 ± 8.26	14.83 ± 5.27	18.09 ± 10.12	p < 0.001; C,D>A B > D,A	p = 0.006; C,B,D > A
	RRA	12.57 ± 4.58	13.94 ± 5.08	17.26 ± 6.54	19.03 ± 7.15	16.95 ± 6.84	20.99 ± 9.15	16.81 ± 6.64	17.57 ± 6.45	p < 0.001; B,C,D > A	p = 0.001; C,D > A B > D,A
	LRA	11.91 ± 3.63	12.2 ± 4.24	16.2 ± 5.46	15.26 ± 6.21	17.44 ± 8.52	16.41 ± 8.54	15.87 ± 5.55	14.89 ± 6.97	p < 0.001; C,D>A B > D,A	p = 0.021; B > A

CT attenuation and CNR, SNR given as means ± standard deviation.

LB – Linearly Blended, VMI – Virtual Monoenergetic Images, MAR – Metal Artifacts Reduction, ASIR – Adaptative Statistical Reconstructions, CNR – Contrast-to-Noise Ratio, SNR – Signal-to-Noise Ratio.

$$AI = \sqrt{SD1^2 - SD2^2}$$

where SD1 is the standard deviation in ROI placed in max. artifacts, and SD2 is standard deviation in region without artifacts.

2.4. Assessment of luminal diameters, artery stenosis and image quality

Measurements were conducted using the following reconstructions: LB, VMI 60 keV, MAR 60 keV, ASIR 60 % 60 keV, by two independent readers blinded to the type of reconstruction (a specialist with 6 years of experience, a radiology resident with 3 years of experience) at one-week intervals. Measurements of each stented target vessel were conducted at the distal end of the stent and in the section with the greatest stenosis of the vessel in the proximal section of the stent. Multiplanar reconstructions (MPRs) were used for all measurements for the appropriate angulation of vessels. Because of the expected (and described in the literature [45,46]) effect of the preset window settings on the perception of the vessel width, the preset window settings (W, 400 HU; L, 100 HU) were not modified.

After measurements were performed in a patient, the readers were asked to rate the overall image quality of the reviewed reconstruction on the 5-point Likert scale:

1. Artifacts preventing the assessment of stents proximally and distally,
2. Artifacts preventing the assessment of stents proximally or distally,
3. Significant artifacts preventing the assessment of one of the stent walls,
4. Minimal artifacts with no significant effect on the examination quality,
5. High-quality picture with no artifacts,

The assessment of the intra-reader agreement was performed by a repeated evaluation of 20 % of measurements from randomly selected patients two weeks after the previous evaluation. The assessment of the inter-reader agreement was also performed.

2.5. Statistical analysis

A repeated-measures ANOVA test (followed by paired t-tests with Bonferroni correction as a post-hoc procedure) was used to compare four repeated measures (LB vs VMI vs MAR vs ASIR) of quantitative variables. The concordance of measurements of quantitative variables was assessed with ICC (Intraclass Correlation Coefficient) type 2 (according to the Shrout & Fleiss classification). Significance level for all statistical tests was set at 0.05. R Statistical Software (v4.1.2; R Core Team 2021) was used for computations.
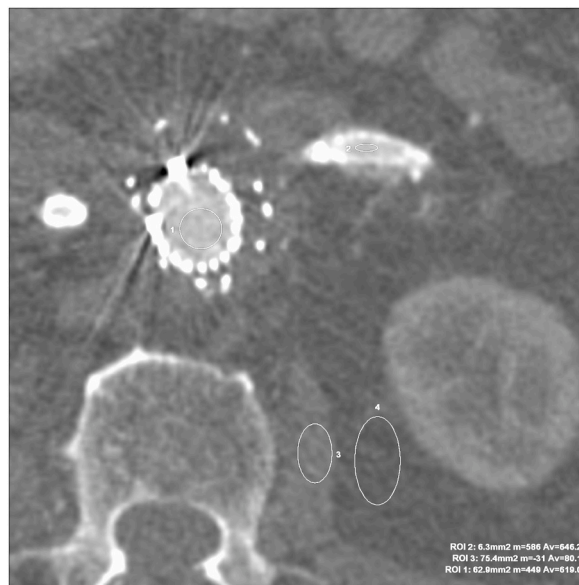

Fig. 1. VMI ASIR 60 keV axial images for the objective evaluation of image quality. The marked regions were ROIs in regions without artifacts in the main stentgraft module (ROI 1 – Av. 619 HU), LRA (ROI 2 – Av. 646,2 HU), psoas muscle (ROI 3 – Av. 80,1 HU), adipose tissue (ROI 4 – Av. −110,1 HU).

3. Results

3.1. Patient population

A total of 28 patients (5 women, 23 men, mean age 72.1 years, range 62.9–86.9) were included in the study. All examinations took place 30 days after the procedure of stentgraft implantation due to abdominal/thoracoabdominal aortic aneurysms. The examination is performed as part of the routine diagnostic protocol following EVAR procedures [3,4]. During the study, 108 stents in the following target arteries were assessed: 25 in the TC, 28 in the SMA, 28 in the RRA and 27 in the LRA. One patient had no stents in either the TC or in the LRA (TC not covered by stentgraft, LRA with clotting). In 2 patients, the stentgraft was implanted below the TC. The patients' mean body mass index was 28 ± 3.3.

3.2. Objective image quality

The results of objective image quality of reconstructions: LB, VMI 60 keV, MAR VMI 60 keV, ASIR 60 keV are summarized in Table 1. CT attenuation measurements in each of the analyzed vessels (aorta, TC SMA, RRA, LRA, RCIA) demonstrated the lowest mean values in the LB reconstruction (statistically significant differences, $p < 0.05$). Noise defined as SD in the subcutaneous adipose tissue was the lowest in the LB reconstructions, although the CNR and SNR values measured in no-artifact and maximum-artifact areas were the lowest for the LB reconstruction as well ($p < 0.05$). The highest CNR and SNR in target vessels were noted for the MAR VMI 60 keV reconstructions, in both no-artifact and maximum-artifact areas. Fig. 1 shows an example of ROI positioning.

Analysis of CNR in VMI 40–90 keV showed the highest CNR values for VMI with a low photon energy (40 keV). In contrast, SNR was the highest for the VMI 70 keV reconstructions. The correlations of CNR and SNR with VMI 40–90 keV, within TC shown as an example, are presented in Fig. 2 (A–D).

The results of analysis of differences in CT numbers in regions without artifacts and in maximum artifacts in vessels and Artifact Indexes summarized in Table 2. The ΔHU values of the artifacts were lowest in linearly blended images (40.41 ± 23.92 HU) and highest in the MAR reconstructions (67.245 ± 61.13). The artifact index was highest in the VMI 60 keV images (173.78 ± 52.50) and lowest in linearly blended images (116.81 ± 65.19).

3.3. Stent lumen diameter assessment

Vessel diameters measured by 2 readers at two points (maximum stenosis at proximal 2/3 of the stent length, as well as the distal end) in the LB, VMI 60 keV, MAR VMI 60 keV and ASIR 60 keV reconstructions did not reveal any statistically significant differences ($p > 0.05$). Table 3 and Fig. 3 present examples of analyses performed for RRA measurements.
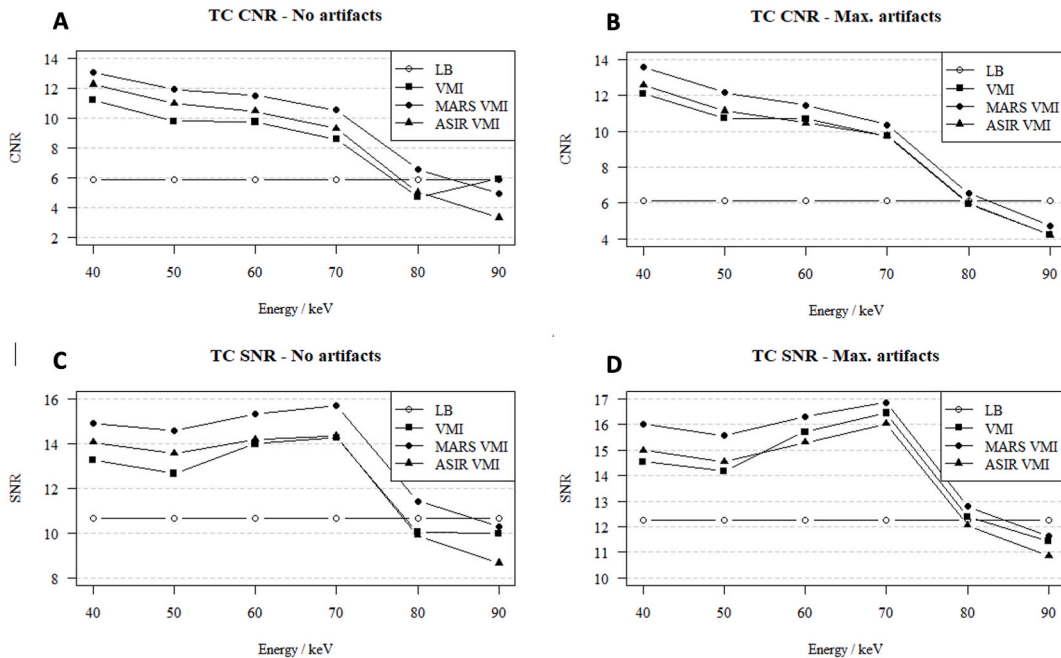

Fig. 2. (A–D). Contrast-to-noise ratio (A, B) and signal to noise ratio (C, D) in no-artifact and in maximum-artifact measurements in the celiac trunk in the LB, VMI, ASIR 60 %, MAR reconstructions (monoenergetic images 40–90 keV).

Table 2

The comparison of △HU and Artifact Index in evaluated reconstructions.

Parameter	LB	VMI 60	MARS VMI 60	ASIR 60 % VMI 60
ΔHU	40,41 ± 23,92	63,83 ± 33,43	67,245 ± 61,13	51,26 ± 43,03
Artifact Index	116,81 ± 65,19	173,78 ± 52,50	140,74 ± 35,72	156,75 ± 65,73

$\triangle HU = HU_{max\ artifacts} - HU_{no\ artifacts}$.

△HU and Artifact Index given as means ± standard deviation.

LB – Linearly Blended, VMI – Virtual Monoenergetic Images, MAR – Metal Artifacts Reduction, ASIR – Adaptative Statistical Reconstructions.

Table 3

Comparison of measurements of the right renal artery stent width in LB, VMI, MARS VMI, ASIR VMI.

Parameter	Measurement	Mean	SD	Median	Min	Max	Q1	Q3	p
RRA prox.	LB	3.21	0.52	3.15	2.2	4.5	3.00	3.50	p = 0.875
	VMI	3.14	0.54	3.10	2.2	4.5	3.00	3.35	
	MARS VMI	3.20	0.55	3.05	2.2	4.1	2.80	3.65	
	ASIR 60 % VMI	3.20	0.51	3.20	1.8	4.4	3.00	3.42	
RRA dist.	LB	3.50	0.83	3.35	2.4	5.7	3.08	3.73	p = 0.545
	VMI	3.52	0.87	3.35	2.4	5.7	3.05	3.75	
	MARS VMI	3.56	0.92	3.50	2.1	5.5	2.70	4.22	
	ASIR 60 % VMI	3.62	0.92	3.45	2.5	6.0	2.90	3.87	

p - repeated measures ANOVA.

LB – Linearly Blended, VMI – Virtual Monoenergetic Images, MAR – Metal Artifacts Reduction, ASIR – Adaptative Statistical Reconstructions, SD – Standard Deviation, Q1 – Quartile 1, Q3 – Quartile 3.
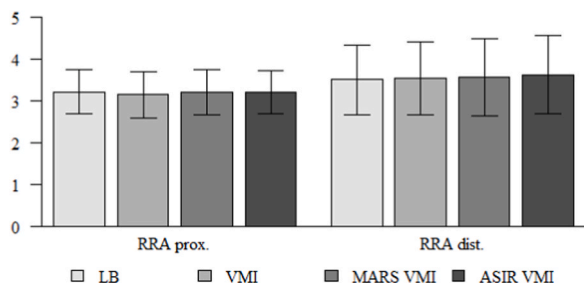

Fig. 3. Comparison of measurements of the right renal artery stent width in the proximal part and distal end of in LB, VMI, MARS VMI, ASIR 60 % VMI.

3.4. Subjective image quality

Detailed results are summarized in Table 4 and Fig. 4. Data in tables are mean of ratings of both readers. Overall, subjective image quality was the lowest for MAR VMI 60 keV (mean rating 1.57 ± 0.5), lower in a statistically significant manner compared with LB and VMI (p < 0.001). The highest subjective image quality was offered by ASIR VMI 60 keV (mean 4.25 ± 0.44). Fig. 4 presents differences in image quality of the ASIR VMI 60 keV and MAR VMI 60 keV reconstructions.

3.5. Intra-reader, inter-reader reliability

The repeatability of the vessel diameter intra-reader measurements is summarized in Table 5. The concordance of most measurements was excellent or, at worst, fair. The concordance of inter-reader measurements was fair to excellent.

Table 4

Subjective image quality (2 readers).

Rating	LB - A	VMI - B	MARS VMI - C	ASIR VMI - D	p
mean ± SD	3.96 ± 0.58	4 ± 0.67	1.57 ± 0.5	4.25 ± 0.44	p < 0.001
median	4	4	2	4	
quartiles 1–3	4–4	4–4	1–2	4–4.25	D > A,C B,A > C

p - Friedman test + post-hoc analysis (Wilcoxon paired tests with Bonferroni correction).

LB – Linearly Blended, VMI – Virtual Monoenergetic Images, MAR – Metal Artifacts Reduction, ASIR – Adaptative Statistical Reconstructions, SD – Standard Deviation, Q1 – Quartile 1, Q3 – Quartile 3.
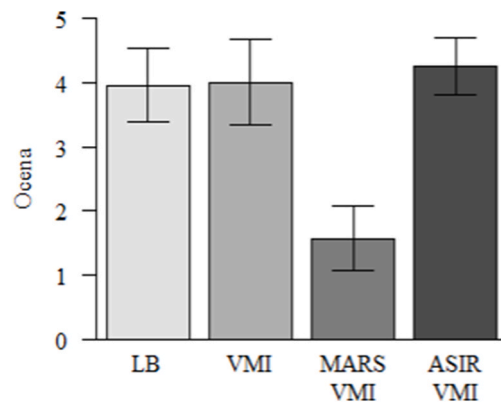
Fig. 4. Subjective image quality of reconstructions (data are mean of 2-readers ratings).

Table 5
Intra-reader agreement on measurements.

Parameter	Measurement 1 (mean ± SD)	Measurement 2 (mean ± SD)	ICC	95 % CI		Agreement (Cicchetti)	Agreement (Koo & Li)
TC prox.	4.89 ± 1.2	4.56 ± 0.99	0.707	0.133	0.932	Good	Fair
TC dist.	5.64 ± 1.61	5.71 ± 1.66	0.975	0.893	0.995	Excellent	Excellent
SMA prox.	4.94 ± 1.21	4.87 ± 1	0.897	0.660	0.973	Excellent	Good
SMA dist.	5.56 ± 1.68	5.42 ± 1.65	0.990	0.945	0.998	Excellent	Excellent
RRA prox.	3.06 ± 0.25	3.11 ± 0.53	0.523	−0.526	0.872	Fair	Fair
RRA dist.	3.38 ± 0.66	3.29 ± 0.59	0.583	−0.001	0.875	Fair	Fair
LRA prox.	3.37 ± 0.46	3.18 ± 0.42	0.526	−0.084	0.865	Fair	Fair
LRA dist.	3.79 ± 0.71	3.63 ± 0.73	0.796	0.364	0.949	Excellent	Good

TC – Celiac trunk, SMA – Superior mesenteric artery, RRA – Right renal artery, LRA – Left renal artery, SD – Standard Deviation, ICC – Interclass Correlation Coefficient, CI – Confidence Interval.

4. Discussion

Our comparison between the 40–90 keV VMI, MAR and ASIR images revealed slight differences in CNR, SNR and noise levels between these reconstructions. Based on the objective image quality parameters (highest CNR in 40 keV images, highest SNR in 70 keV images) and prior studies, which reported improvements in the quantitative image quality in low-energy VMIs [34,47–51], we chose 60 keV images to assess the subjective image quality of the above-mentioned reconstructions. There is published literature in which the highest SNR and CNR values in angiography examinations were obtained with VMI 60 keV images [52–54]. In our view, the selected value of 60 keV allows assessing both target vessels and endoleaks, the latter of which are the main reason for repeated CTA in this group of patients. There are a number of studies demonstrating the value of low level keV reconstructions in detecting endoleaks [24, 28,55–57]. Therefore, we considered VMI 60 keV reconstructions as the optimal compromise in assessing target vessels and endoleaks. Analyses performed did not demonstrate any statistically significant differences in the vessel diameters measured in those reconstructions. Measurements within stents in no-artifact and maximum-artifact areas showed similar differences in CT attenuation, with higher mean values for the measurements of areas with artifacts. This translated into the SNR and CNR values which were higher for the measurements of areas with artifacts. This phenomenon is associated with beam hardening artifacts, contributing to an increase of the mean beam energy [58]. Use of iterative algorithms provided superior image quality and reduced noise compared with standard LB and monoenergetic reconstructions. Therefore, the use of ASIR protocols can efficiently improve the subjective and objective image quality by reducing image noise and may ultimately permit reduction of radiation dose in CTA.

In contrast to what we expected, the parameters of the quantitative analysis of examinations, reaching the highest values for the MAR VMI 60 keV reconstruction, were opposite to the results of the qualitative analysis of examinations, in which that type of reconstruction obtained the lowest score. Despite the reduced image noise and high scores in the quantitative assessment, the considerable number of artifacts in most sections completely prevented the evaluation of stents and of the main stent–graft module (Fig. 5A–D). Blurred stent sections within the main stent–graft module prohibited a reliable assessment of their length and width. In part of the cases another issue was noticed in MAR reconstructions – obscuration of endoleaks and additional artifacts mimicking endoleaks presence (Fig. 6 A, B). The results of this analysis are in accordance with some published studies showing a decreased diagnostic value of angiographic examinations employing the MAR technique [59–61]. Most studies, however, demonstrated increased the quantitative and qualitative parameters with MAR, also in stent imaging [41,62]. Most of the published literature indicated high-VMI (>100 keV) MAR as offering optimal results [51,60,62–65], although its use is associated with a significant decrease in contrast between soft tissue structures and the contrast agent in blood vessels. High VMI values (>100 keV) are generally not recommended for the assessment of the vascular system and negatively impact the possibility of assessing potential vessel
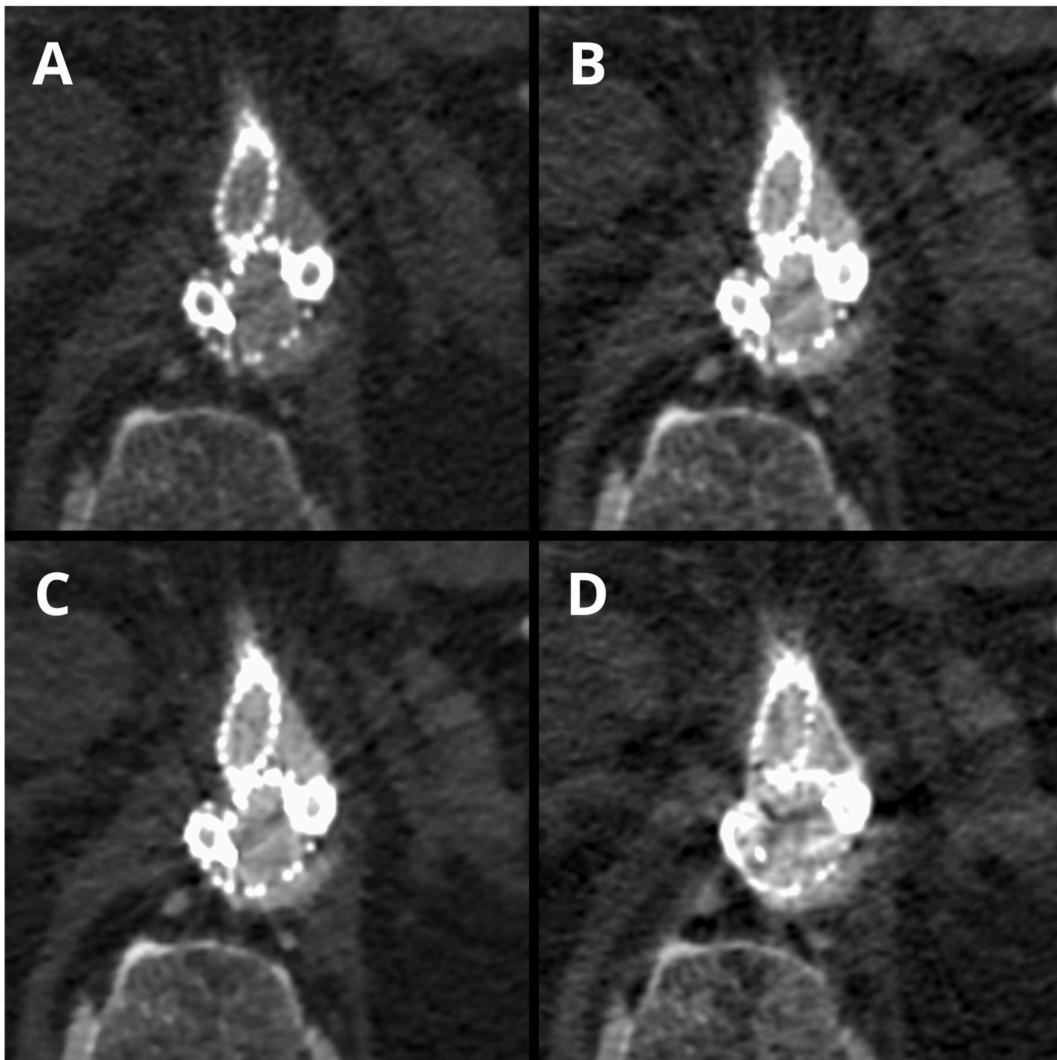
Fig. 5. (A–D). Case presenting differences in the subjective image quality in LB images (A – rated 5-points), VMI 60 keV (B – rated 4-points), VMI ASIR 60 % 60 keV (C – rated 5-points) and VMI MAR 60 keV (D – rated 1-point on Likert scale).

diameters and stenoses [32,66,67]. Our results of the qualitative evaluation of the MAR reconstructions, differing from a large part of the available literature, may be due to the difference in the equipment (data acquisition technique) and MAR software used, both originating from different manufacturers.

The results of this study should be considered alongside its limitations. First, the patient population was relatively small. Second, the results are specific to the DECT acquisition and postprocessing technique, as well as algorithms specific to one vendor. Third, for the subjective image quality assessment, we chose 60 keV virtual monoenergetic images, based on the objective image quality results (with high CNR and SNR values at 60 keV) and general recommendations regarding DECT angiography [11,21–26]. Therefore, the results (especially those of the MAR qualitative analysis) should be considered within the narrow kiloelectron volt level range used (60 keV). Further investigations could elucidate if different kiloelectron volt levels may significantly impact the subjective image quality.

5. Conclusion

In conclusion, the use of MAR algorithms caused a decrease in the diagnostic value of the examination (a large decrease in the parameters of qualitative image assessment) by generating artifacts prohibiting stent assessment. The use of iterative algorithms increased the qualitative and quantitative image parameters compared with the VMI and LB reconstructions and should be considered for inclusion in the diagnostic protocols. The type of reconstruction used did not significantly affect the measurement of stent width in target vessels in patients after f/brEVAR.
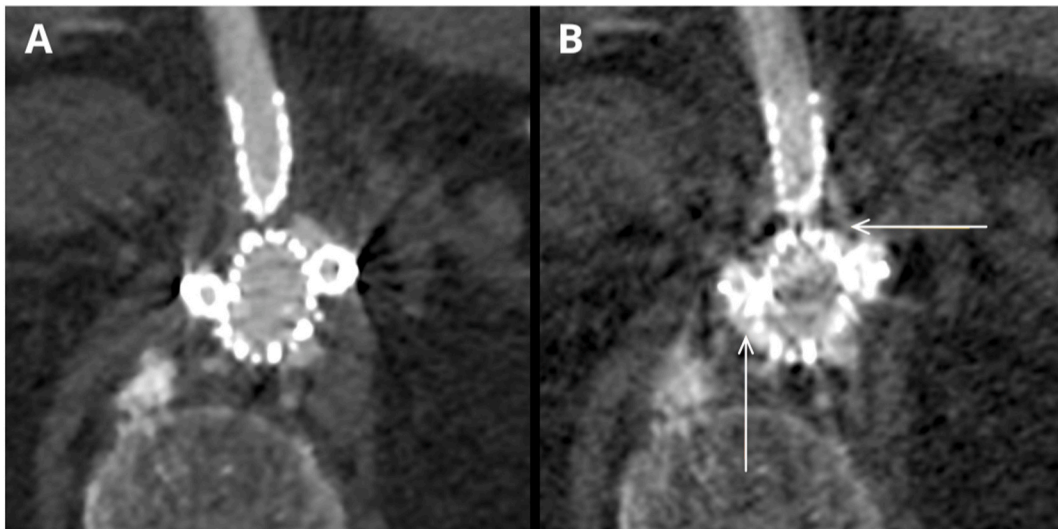
Fig. 6. (A, B). Case presenting type III endoleak in the same slice in VMI ASIR 60 % 60 keV (A) and VMI MAR 60 keV (B). MAR images show simultaneous obscuration of the endoleak (horizontal arrow) and additional artifacts mimicking the presence of the endoleak (vertical arrow).

Data availability statement

The data associated with our study is confidential due to nature of medical records and imaging studies.

CRediT authorship contribution statement

Wojciech Kazimierczak: Writing – review & editing, Writing – original draft, Visualization, Validation, Supervision, Software, Resources, Project administration, Methodology, Investigation, Formal analysis, Data curation, Conceptualization. **Ewa Nowak:** Investigation. **Natalia Kazimierczak:** Writing – original draft. **Tomasz Jankowski:** Writing – review & editing. **Agnieszka Jankowska:** Validation. **Zbigniew Serafin:** Supervision, Project administration.

Declaration of competing interest

The authors declare that they have no known competing financial interests or personal relationships that could have appeared to influence the work reported in this paper.

Acknowledgements

None.

References

[1] R.A.P. Scott, S.G. Bridgewater, H.A. Ashton, Randomized clinical trial of screening for abdominal aortic aneurysm in women, Br. J. Surg. 89 (2002), https://doi.org/10.1046/j.0007-1323.2001.02014.x.
[2] J.T. McPhee, J.S. Hill, M.H. Eslami, The impact of gender on presentation, therapy, and mortality of abdominal aortic aneurysm in the United States, 2001-2004, J. Vasc. Surg. 45 (2007), https://doi.org/10.1016/j.jvs.2007.01.043.
[3] A. Wanhainen, F. Verzini, I. van Herzeele, E. Allaire, M. Bown, T. Cohnert, F. Dick, J. van Herwaarden, C. Karkos, M. Koelemay, T. Kölbel, I. Loftus, K. Mani, G. Melissano, J. Powell, Z. Szeberin, Esvs Guidelines Committee, G.J. de Borst, N. Chakfe, S. Debus, R. Hinchliffe, S. Kakkos, I. Koncar, P. Kolh, J.S. Lindholt, M. de Vega, F. Vermassen, Document reviewers, M. Björck, S. Cheng, R. Dalman, L. Davidovic, K. Donas, J. Earnshaw, H.H. Eckstein, J. Golledge, S. Haulon, T. Mastracci, R. Naylor, J.B. Ricco, H. Verhagen, Editor's choice – European society for vascular surgery (ESVS) 2019 clinical practice guidelines on the management of abdominal aorto-iliac artery aneurysms, Eur. J. Vasc. Endovasc. Surg. 57 (2019), https://doi.org/10.1016/j.ejvs.2018.09.020.
[4] E.L. Chaikof, R.L. Dalman, M.K. Eskandari, B.M. Jackson, W.A. Lee, M.A. Mansour, T.M. Mastracci, M. Mell, M.H. Murad, L.L. Nguyen, G.S. Oderich, M.S. Patel, M.L. Schermerhorn, B.W. Starnes, The Society for Vascular Surgery practice guidelines on the care of patients with an abdominal aortic aneurysm, J. Vasc. Surg. 67 (2018), https://doi.org/10.1016/j.jvs.2017.10.044.
[5] F.A.B. Grimme, C.J. Zeebregts, E.L.G. Verhoeven, F. Bekkema, M.M.J.P. Reijnen, I.F.J. Tielliu, Visceral stent patency in fenestrated stent grafting for abdominal aortic aneurysm repair, J. Vasc. Surg. 59 (2014), https://doi.org/10.1016/j.jvs.2013.08.005.
[6] N.O. Glebova, S. Selvarajah, K.C. Orion, J.H. Black, M.B. Malas, B.A. Perler, C.J. Abularrage, Fenestrated endovascular repair of abdominal aortic aneurysms is associated with increased morbidity but comparable mortality with infrarenal endovascular aneurysm repair, J. Vasc. Surg. (2015), https://doi.org/10.1016/j.jvs.2014.10.025.
[7] N. Troisi, K.P. Donas, M. Austermann, J. Tessarek, T. Umscheid, G. Torsello, Secondary procedures after aortic aneurysm repair with fenestrated and branched endografts, J. Endovasc. Ther. 18 (2011), https://doi.org/10.1583/10-3274.1.
[8] D. Fleischmann, Multiple detector-row CT angiography of the renal and mesenteric vessels, Eur. J. Radiol. (2003), https://doi.org/10.1016/S0720-048X(02)00364-9.

[9] W. Kazimierczak, N. Kazimierczak, P. Ratajczak, W. Leszczyński, Ł. Bryl, A. Lemanowicz, Z. Serafin, Contemporary imaging methods for the follow-up after endovascular abdominal aneurysm repair: a review, Wideochirurgia Inne Tech. Malo Inwazyjne 14 (2019), https://doi.org/10.5114/wiitm.2018.78973.

[10] I. Vlahos, R. Chung, A. Nair, R. Morgan, Dual-energy CT: vascular applications, AJR Am. J. Roentgenol. 199 (2012), https://doi.org/10.2214/ajr.12.9114.

[11] M. Michalska, W. Kazimierczak, W. Leszczyński, K. Nadolska, Ł. Bryl, Contemporary follow-up imaging after endovascular repair of lower extremity atherosclerotic lesions, Pol. J. Radiol. 83 (2018), https://doi.org/10.5114/pjr.2018.80348.

[12] W. Abdellatif, M.A. Ebada, S. Alkanj, A. Negida, N. Murray, F. Khosa, S. Nicolaou, Diagnostic Accuracy of Dual-Energy CT in Detection of Acute Pulmonary Embolism: A Systematic Review and Meta-Analysis, vol. 72, Canadian Association of Radiologists Journal, 2021, https://doi.org/10.1177/0846537120902062.

[13] C.B. Monti, M. Zanardo, A. Cozzi, S. Schiaffino, P. Spagnolo, F. Secchi, C.N. De Cecco, F. Sardanelli, Dual-energy CT performance in acute pulmonary embolism: a meta-analysis, Eur. Radiol. 31 (2021), https://doi.org/10.1007/s00330-020-07633-8.

[14] S.M. Ko, J.W. Choi, M.G. Song, J.K. Shin, H.K. Chee, H.W. Chung, D.H. Kim, Myocardial perfusion imaging using adenosine-induced stress dual-energy computed tomography of the heart: comparison with cardiac magnetic resonance imaging and conventional coronary angiography, Eur. Radiol. 21 (2011), https://doi.org/10.1007/s00330-010-1897-1.

[15] J.L. Wichmann, R.W. Bauer, M. Doss, W. Stock, T. Lehnert, B. Bodelle, C. Frellesen, T.J. Vogl, J. Matthias Kerl, Diagnostic accuracy of late iodine-enhancement dual-energy computed tomography for the detection of chronic myocardial infarction compared with late gadolinium-enhancement 3-T magnetic resonance imaging, Invest. Radiol. 48 (2013), https://doi.org/10.1097/RLI.0b013e31829d91a8.

[16] T. D'Angelo, G. Cicero, S. Mazziotti, G. Ascenti, M.H. Albrecht, S.S. Martin, A.E. Othman, T.J. Vogl, J.L. Wichmann, Dual energy computed tomography virtual monoenergetic imaging: technique and clinical applications, Br. J. Radiol. 92 (2019), https://doi.org/10.1259/bjr.20180546.

[17] S.S. Martin, J.L. Wichmann, J.E. Scholtz, D. Leithner, T. D'Angelo, H. Weyer, C. Booz, L. Lenga, T.J. Vogl, M.H. Albrecht, Noise-Optimized virtual monoenergetic dual-energy CT improves diagnostic accuracy for the detection of active arterial bleeding of the abdomen, J. Vasc. Intervent. Radiol. 28 (2017), https://doi.org/10.1016/j.jvir.2017.06.011.

[18] J.L. Wichmann, R.W. Katzberg, S.E. Litwin, P.L. Zwerner, C.N. De Cecco, T.J. Vogl, P. Costello, U.J. Schoepf, Contrast-induced nephropathy, Circulation 132 (2015), https://doi.org/10.1161/CIRCULATIONAHA.115.014672.

[19] A. Parakh, F. Macri, D. Sahani, Dual-energy computed tomography: dose reduction, series reduction, and contrast load reduction in dual-energy computed tomography, Radiol. Clin. 56 (2018), https://doi.org/10.1016/j.rcl.2018.03.002.

[20] T. Henzler, C. Fink, S.O. Schoenberg, U.J. Schoepf, Dual-energy CT: radiation dose aspects, AJR Am. J. Roentgenol. 199 (2012), https://doi.org/10.2214/ajr.12.9210.

[21] D. Leithner, S. Mahmoudi, J.L. Wichmann, S.S. Martin, L. Lenga, M.H. Albrecht, C. Booz, C.T. Arendt, M. Beeres, T. D'Angelo, B. Bodelle, T.J. Vogl, J.E. Scholtz, Evaluation of virtual monoenergetic imaging algorithms for dual-energy carotid and intracerebral CT angiography: effects on image quality, artefacts and diagnostic performance for the detection of stenosis, Eur. J. Radiol. 99 (2018), https://doi.org/10.1016/j.ejrad.2017.12.024.

[22] T. Hickethier, J. Byrtus, M. Hauger, A.I. Iuga, G. Pahn, D. Maintz, S. Haneder, J. Doerner, Utilization of virtual mono-energetic images (MonoE) derived from a dual-layer spectral detector CT (SDCT) for the assessment of abdominal arteries in venous contrast phase scans, Eur. J. Radiol. 99 (2018), https://doi.org/10.1016/j.ejrad.2017.12.007.

[23] M.D. Agrawal, G.R. Oliveira, S.P. Kalva, D.F. Pinho, R.S. Arellano, D.v. Sahani, Prospective comparison of reduced-iodine-dose virtual monochromatic imaging dataset from dual-energy CT angiography with standard-iodine-dose single-energy CT angiography for abdominal aortic aneurysm, Am. J. Roentgenol. 207 (2016), https://doi.org/10.2214/AJR.15.15814.

[24] S.S. Martin, J.L. Wichmann, H. Weyer, J.E. Scholtz, D. Leithner, A. Spandorfer, B. Bodelle, V. Jacobi, T.J. Vogl, M.H. Albrecht, Endoleaks after endovascular aortic aneurysm repair: improved detection with noise-optimized virtual monoenergetic dual-energy CT, Eur. J. Radiol. 94 (2017), https://doi.org/10.1016/j.ejrad.2017.06.017.

[25] P. Apfaltrer, S. Sudarski, D. Schneider, J.W. Nance, H. Haubenreisser, C. Fink, S.O. Schoenberg, T. Henzler, Value of monoenergetic low-kV dual energy CT datasets for improved image quality of CT pulmonary angiography, Eur. J. Radiol. 83 (2014), https://doi.org/10.1016/j.ejrad.2013.11.005.

[26] S. Leng, L. Yu, J.G. Fletcher, C.H. McCollough, Maximizing iodine contrast-to-noise ratios in abdominal CT imaging through use of energy domain noise reduction and virtual monoenergetic dual-energy CT, Radiology 276 (2015), https://doi.org/10.1148/radiol.2015140857.

[27] T. D'Angelo, G. Vizzari, L.R.M. Lanzafame, F. Pergolizzi, S. Mazziotti, M. Gaeta, F. Costa, G. Di Bella, T.J. Vogl, C. Booz, A. Micari, A. Blandino, Spectral CT imaging of prosthetic valve embolization after transcatheter aortic valve implantation, Diagnostics 13 (2023), https://doi.org/10.3390/diagnostics13040678.

[28] W. Kazimierczak, N. Kazimierczak, A. Lemanowicz, E. Nowak, A. Migdalski, A. Jawien, T. Jankowski, Z. Serafin, Improved detection of endoleaks in virtual monoenergetic images in dual-energy CT angiography following EVAR, Acad. Radiol. (2023), https://doi.org/10.1016/j.acra.2023.03.018.

[29] C.A. Coursey, R.C. Nelson, D.T. Boll, E.K. Paulson, L.M. Ho, A.M. Neville, D. Marin, R.T. Gupta, S.T. Schindera, Dual-energy multidetector CT: how does it work, what can it tell us, and when can we use it in abdominopelvic imaging? Radiographics 30 (2010) https://doi.org/10.1148/rg.304095175.

[30] M.H. Albrecht, C.N. De Cecco, J.W. Nance, A. Varga-Szemes, D. De Santis, C. Tesche, G. Apfaltrer, P.L. von Knebel Doeberitz, B. Jacobs, T.J. Vogl, U. Joseph Schoepf, Cardiac dual-energy CT applications and clinical impact, Curr Radiol Rep 5 (2017), https://doi.org/10.1007/s40134-017-0237-5.

[31] S. Mangold, P.M. Cannaó, U.J. Schoepf, J.L. Wichmann, C. Canstein, S.R. Fuller, G. Muscogiuri, A. Varga-Szemes, K. Nikolaou, C.N. De Cecco, Impact of an advanced image-based monoenergetic reconstruction algorithm on coronary stent visualization using third generation dual-source dual-energy CT: a phantom study, Eur. Radiol. 26 (2016), https://doi.org/10.1007/s00330-015-3997-4.

[32] T. Hickethier, B. Baeßler, J.R. Kroeger, J. Doerner, G. Pahn, D. Maintz, G. Michels, A.C. Bunck, Monoenergetic reconstructions for imaging of coronary artery stents using spectral detector CT: in-vitro experience and comparison to conventional images, J Cardiovasc Comput Tomogr 11 (2017), https://doi.org/10.1016/j.jcct.2016.12.005.

[33] C.N. De Cecco, A. Darnell, M. Rengo, G. Muscogiuri, D. Bellini, C. Ayuso, A. Laghi, Dual-energy CT: oncologic applications, AJR Am. J. Roentgenol. 199 (2012), https://doi.org/10.2214/ajr.12.9207.

[34] D. Leithner, J.L. Wichmann, T.J. Vogl, J. Trommer, S.S. Martin, J.E. Scholtz, B. Bodelle, C.N. de Cecco, T. Duguay, J.W. Nance, U.J. Schoepf, M.H. Albrecht, Virtual monoenergetic imaging and iodine perfusion maps improve diagnostic accuracy of dual-energy computed tomography pulmonary angiography with suboptimal contrast attenuation, Invest. Radiol. 52 (2017), https://doi.org/10.1097/RLI.0000000000000387.

[35] S. Singh, M.K. Kalra, J. Hsieh, P.E. Licato, S. Do, H.H. Pien, M.A. Blake, Abdominal CT: Comparison of adaptive statistical iterative and filtered back projection reconstruction techniques, Radiology 257 (2010), https://doi.org/10.1148/radiol.10092212.

[36] J. Leipsic, T.M. LaBounty, B. Heilbron, J.K. Min, G.B.J. Mancini, F.Y. Lin, C. Taylor, A. Dunning, J.P. Earls, Adaptive statistical iterative reconstruction: assessment of image noise and image quality in coronary CT angiography, Am. J. Roentgenol. 195 (2010), https://doi.org/10.2214/AJR.10.4285.

[37] C.M. Chen, S.Y. Chu, M.Y. Hsu, Y.L. Liao, H.Y. Tsai, Low-tube-voltage (80 kVp) CT aortography using 320-row volume CT with adaptive iterative reconstruction: lower contrast medium and radiation dose, Eur. Radiol. 24 (2014), https://doi.org/10.1007/s00330-013-3027-3.

[38] G. Böning, R.A. Rotzinger, J.F. Kahn, P. Freyhardt, D.M. Renz, M. Maurer, F. Streitparth, Tailored CT angiography in follow-up after endovascular aneurysm repair (EVAR): combined dose reduction techniques, Acta Radiol 59 (2018), https://doi.org/10.1177/0284185118756952.

[39] A. C, N. M, O. E, S.S. A, Reasons and treatment options for late type II endoleaks, Cardiovasc. Intervent. Radiol. 42 (2019).

[40] S.W. Stavropoulos, H. Marin, R.M. Fairman, J.P. Carpenter, H.I. Litt, M. Itkin, T.W.I. Clark, Recurrent endoleak detection and measurement of aneurysm size with CTA after coil embolization of endoleaks, J. Vasc. Intervent. Radiol. 16 (2005), https://doi.org/10.1097/01.RVI.0000175900.61777.9A.

[41] M.A.A.D. Ragusi, R.W. van der Meer, R.M.S. Joemai, J. van Schaik, C.S.P. van Rijswijk, Evaluation of CT angiography image quality acquired with single-energy metal artifact reduction (SEMAR) algorithm in patients after complex endovascular aortic repair, Cardiovasc. Intervent. Radiol. 41 (2018), https://doi.org/10.1007/s00270-017-1812-0.

[42] J. Boos, J. Fang, B.H. Heidinger, V. Raptopoulos, O.R. Brook, Dual energy CT angiography: pros and cons of dual-energy metal artifact reduction algorithm in patients after endovascular aortic repair, Abdominal Radiology 42 (2017), https://doi.org/10.1007/s00261-016-0973-7.

[43] A. Blum, J.B. Meyer, A. Raymond, M. Louis, O. Bakour, R. Kechidi, A. Chanson, P. Gondim-Teixeira, CT of hip prosthesis: new techniques and new paradigms, Diagn Interv Imaging 97 (2016), https://doi.org/10.1016/j.diii.2016.07.002.

[44] M.N. Bongers, C. Schabel, C. Thomas, R. Raupach, M. Notohamiprodjo, K. Nikolaou, F. Bamberg, Comparison and combination of dual-energy- and iterative-based metal artefact reduction on hip prosthesis and dental implants, PLoS One 10 (2015), https://doi.org/10.1371/journal.pone.0143584.

[45] T. D'Angelo, A.M. Bucher, L. Lenga, C.T. Arendt, J.L. Peterke, D. Caruso, S. Mazziotti, A. Blandino, G. Ascenti, A.E. Othman, S.S. Martin, D. Leithner, T.J. Vogl, J. L. Wichmann, Optimisation of window settings for traditional and noise-optimised virtual monoenergetic imaging in dual-energy computed tomography pulmonary angiography, Eur. Radiol. 28 (2018), https://doi.org/10.1007/s00330-017-5059-6.

[46] T. D'Angelo, L. Lenga, C.T. Arendt, A.M. Bucher, J.L. Peterke, D. Caruso, S. Mazziotti, G. Ascenti, A. Blandino, A.E. Othman, S.S. Martin, M.H. Albrecht, B. Bodelle, T.J. Vogl, J.L. Wichmann, Carotid and cerebrovascular dual-energy computed tomography angiography: optimization of window settings for virtual monoenergetic imaging reconstruction, Eur. J. Radiol. 130 (2020), https://doi.org/10.1016/j.ejrad.2020.109166.

[47] K.L. Grant, T.G. Flohr, B. Krauss, M. Sedlmair, C. Thomas, B. Schmidt, Assessment of an advanced image-based technique to calculate virtual monoenergetic computed tomographic images from a dual-energy examination to improve contrast-to-noise ratio in examinations using iodinated contrast media, Invest. Radiol. 49 (2014), https://doi.org/10.1097/RLI.0000000000000060.

[48] D.B. Husarik, S. Gordic, L. Desbiolles, B. Krauss, S. Leschka, S. Wildermuth, H. Alkadhi, Advanced virtual monoenergetic computed tomography of hyperattenuating and hypoattenuating liver lesions: ex-vivo and patient experience in various body sizes, Invest. Radiol. 50 (2015), https://doi.org/10.1097/RLI.0000000000000171.

[49] M.H. Albrecht, J. Trommer, J.L. Wichmann, J.E. Scholtz, S.S. Martin, T. Lehnert, T.J. Vogl, B. Bodelle, Comprehensive comparison of virtual monoenergetic and linearly blended reconstruction techniques in third-generation dual-source dual-energy computed tomography angiography of the thorax and abdomen, Invest. Radiol. 51 (2016), https://doi.org/10.1097/RLI.0000000000000272.

[50] B. Dane, H. Patel, T. O'Donnell, F. Girvin, G. Brusca-Augello, J.B. Alpert, B. Niu, M. Attia, J. Babb, J.P. Ko, Image quality on dual-energy CTPA virtual monoenergetic images: quantitative and qualitative assessment, Acad. Radiol. 25 (2018), https://doi.org/10.1016/j.acra.2017.12.012.

[51] V. Dunet, M. Bernasconi, S.D. Hajdu, R.A. Meuli, R.T. Daniel, J.B. Zerlauth, Impact of metal artifact reduction software on image quality of gemstone spectral imaging dual-energy cerebral CT angiography after intracranial aneurysm clipping, Neuroradiology 59 (2017), https://doi.org/10.1007/s00234-017-1871-6.

[52] S. Sudarski, P. Apfaltrer, J.W. Nance, D. Schneider, M. Meyer, S.O. Schoenberg, C. Fink, T. Henzler, Optimization of keV-settings in abdominal and lower extremity dual-source dual-energy CT angiography determined with virtual monoenergetic imaging, Eur. J. Radiol. 82 (2013), https://doi.org/10.1016/j.ejrad.2013.04.040.

[53] M.A. Delesalle, F. Pontana, A. Duhamel, J.B. Faivre, T. Flohr, N. Tacelli, J. Remy, M. Remy-Jardin, Spectral Optimization of Chest CT Angiography with Reduced Iodine Load: Experience in 80 Patients Evaluated with Dual-Source, vol. 267, dual-energy CT, Radiology, 2013, https://doi.org/10.1148/radiol.12120195.

[54] D. Schneider, P. Apfaltrer, S. Sudarski, J.W. Nance, H. Haubenreisser, C. Fink, S.O. Schoenberg, T. Henzler, Optimization of kiloelectron volt settings in cerebral and cervical dual-energy CT angiography determined with virtual monoenergetic imaging, Acad. Radiol. 21 (2014), https://doi.org/10.1016/j.acra.2013.12.006.

[55] P. Stolzmann, T. Frauenfelder, T. Pfammatter, N. Peter, H. Scheffel, M. Lachat, B. Schmidt, B. Marincek, H. Alkadhi, T. Schertler, Endoleaks after endovascular abdominal aortic aneurysm repair: detection with dual-energy dual-source CT, Radiology 249 (2008), https://doi.org/10.1148/radiol.2483080193.

[56] L. Flors, C. Leiva-Salinas, P.T. Norton, J.T. Patrie, K.D. Hagspiel, Endoleak detection after endovascular repair of thoracic aortic aneurysm using dual-source dual-energy CT: suitable scanning protocols and potential radiation dose reduction, Am. J. Roentgenol. 200 (2013), https://doi.org/10.2214/AJR.11.8033.

[57] K.E. Maturen, R.K. Kaza, P.S. Liu, L.E. Quint, S.H. Khalatbari, J.F. Platt, Sweet spot" for endoleak detection: optimizing contrast to noise using low kev reconstructions from fast-switch kVp dual-energy CT, J. Comput. Assist. Tomogr. 36 (2012), https://doi.org/10.1097/RCT.0b013e31824258cb.

[58] E. Pessis, R. Campagna, J.M. Sverzut, F. Bach, M. Rodallec, H. Guerini, A. Feydy, J.L. Drapé, Virtual monochromatic spectral imaging with fast kilovoltage switching: reduction of metal artifacts at CT, Radiographics 33 (2013), https://doi.org/10.1148/rg.332125124.

[59] A. de Crop, J. Casselman, T. van Hoof, M. Dierens, E. Vereecke, N. Bossu, J. Pamplona, K. D'Herde, H. Thierens, K. Bacher, Analysis of metal artifact reduction tools for dental hardware in CT scans of the oral cavity: kVp, iterative reconstruction, dual-energy CT, metal artifact reduction software: does it make a difference? Neuroradiology 57 (2015) https://doi.org/10.1007/s00234-015-1537-1.

[60] J. Fang, D. Zhang, C. Wilcox, B. Heidinger, V. Raptopoulos, A. Brook, O.R. Brook, Metal implants on CT: comparison of iterative reconstruction algorithms for reduction of metal artifacts with single energy and spectral CT scanning in a phantom model, Abdominal Radiology 42 (2017), https://doi.org/10.1007/s00261-016-1023-1.

[61] D.R. Wayer, N.Y. Kim, B.J. Otto, A.M. Grayev, A.D. Kuner, Unintended consequences: review of new artifacts introduced by iterative reconstruction CT metal artifact reduction in spine imaging, Am. J. Neuroradiol. (2019), https://doi.org/10.3174/ajnr.A6238.

[62] Q. Zhang, H. Zhao, Q. Sun, J. Han, H. Zhang, T. Shan, W. Pan, C. Gu, R. Xu, G. Mao, Clinical evaluation of volume of interest imaging combined with metal artifact reduction reconstruction techniques in coiling and stent assisted coiling during neurointerventional procedures, J. Neurointerventional Surg. 11 (2019), https://doi.org/10.1136/neurintsurg-2018-013886.

[63] K.R. Laukamp, S. Lennartz, V.F. Neuhaus, N. Große Hokamp, R. Rau, M. le Blanc, N. Abdullayev, A. Mpotsaris, D. Maintz, J. Borggrefe, CT metal artifacts in patients with total hip replacements: for artifact reduction monoenergetic reconstructions and post-processing algorithms are both efficient but not similar, Eur. Radiol. 28 (2018), https://doi.org/10.1007/s00330-018-5414-2.

[64] L. Pennig, D. Zopfs, R. Gertz, J. Bremm, C. Zaeske, N. Große Hokamp, E. Celik, L. Goertz, M. Langenbach, T. Persigehl, A. Gupta, J. Borggrefe, S. Lennartz, K. R. Laukamp, Reduction of CT artifacts from cardiac implantable electronic devices using a combination of virtual monoenergetic images and post-processing algorithms, Eur. Radiol. 31 (2021), https://doi.org/10.1007/s00330-021-07746-8.

[65] D. Zopfs, S. Lennartz, L. Pennig, A. Glauner, N. Abdullayev, J. Bremm, N. Große Hokamp, T. Persigehl, C. Kabbasch, J. Borggrefe, K.R. Laukamp, Virtual monoenergetic images and post-processing algorithms effectively reduce CT artifacts from intracranial aneurysm treatment, Sci. Rep. 10 (2020), https://doi.org/10.1038/s41598-020-63574-8.

[66] S. van Hedent, N. Große Hokamp, R. Kessner, R. Gilkeson, P.R. Ros, A. Gupta, Effect of virtual monoenergetic images from spectral detector computed tomography on coronary calcium blooming, J. Comput. Assist. Tomogr. 42 (2018), https://doi.org/10.1097/RCT.0000000000000811.

[67] P. Gruschwitz, B. Petritsch, A. Schmid, A.M.A. Schmidt, J.-P. Grunz, P.J. Kuhl, J.F. Heidenreich, H. Huflage, T.A. Bley, A. Kosmala, Noise-optimized virtual monoenergetic reconstructions of dual-energy CT angiographies improve assessability of the lower leg arterial segments in peripheral arterial occlusive disease, Radiography 29 (2023) 19–27, https://doi.org/10.1016/j.radi.2022.09.002.